Radiance Monte-Carlo for application of the Radiative Transport Equation in the inverse problem of Diffuse Optical Tomography

Samuel Powell[a], Roman Hochuli[a], and Simon R. Arridge[b]

[a]Department of Medical Physics & Biomedical Engineering,, University College London, Gower Street, LONDON, WC1E 6BT, UK.
[b]Department of Computer Science, University College London, Gower Street, LONDON, WC1E 6BT, UK.

ABSTRACT

We introduce a new Monte-Carlo technique to estimate the radiance distribution in a medium according to the radiative transport equation (RTE). We demonstrate how to form gradients of the forward model, and thus how to employ this technique as part of the inverse problem in Diffuse Optical Tomography (DOT). Use of the RTE over the more typical application of the diffusion approximation permits accurate modelling in the case of short source-detector separation and regions of low scattering, in addition to providing time-domain information without extra computational effort over continuous-wave solutions.

Keywords: Diffuse Optical Tomography, Radiative Transport Equation, Monte-Carlo Techniques, Inverse Problems, Image Reconstruction

1. INTRODUCTION

A number of biomedical imaging modalities have been developed to image the spatially varying optical properties of biological tissues from measurements of light transmission through the medium. The archetypal technique is Diffuse Optical Tomography (DOT), in which recovery of the parameters of interest is typically achieved by the solution of a model-based inverse problem, whereby an objective function representing the difference between the measured data and a suitable forward model is minimised.

Owing to its modest computational requirements, the diffusion approximation (DA) to the radiative transport equation (RTE) is the usual choice of forward model for the propagation of light employed in the inverse problem. However, the DA is invalid in many contexts of increasing interest both in DOT and related techniques, including in the case of measurements close to optical sources, and the presence of non-scattering regions such as the CSF layer surrounding the brain. Furthermore, the computational requirements of the DA are significantly increased when time-domain information is required.

Recent advances in parallel computing have made stochastic Monte-Carlo solutions to the RTE viable as a forward model, but until now it has not been shown how MC solutions to the RTE can be properly and efficiently used as part of the inverse problem. In this work we introduce a new Monte-Carlo technique to estimate the radiance distribution in a medium according to the RTE. We demonstrate how to efficiently form gradients of the forward model with respect to the parameters of interest, and thus how to employ this technique as part of the typical model-based inverse problem.

Further author information (send correspondence to S. Powell):
S. Powell: E-mail: s.powell@ucl.ac.uk, Telephone: +44 (0) 20 7679 2073
R. Hochuli: E-mail: r.hochuli@ucl.ac.uk
S. R. Arridge: E-mail: s.arridge@cs.ucl.ac.uk

Optical Tomography and Spectroscopy of Tissue XII, edited by Bruce J. Tromberg, Arjun G. Yodh, Eva Marie Sevick-Muraca, Robert R. Alfano, Proc. of SPIE Vol. 10059, 100590W · © 2017 SPIE
CCC code: 1605-7422/17/$18 · doi: 10.1117/12.2250005

2. THEORY

The Radiative Transport Equation for the propagation of light in a three-dimensional domain is given by

$$\mathcal{L}\phi = q \quad \equiv \quad \left(\frac{1}{c}\frac{\partial}{\partial t} + \hat{\mathbf{s}}\cdot\nabla + \mu_{\mathrm{tr}}\right)\phi(\mathbf{r},\hat{\mathbf{s}},t) - \mu_{\mathrm{s}}(\mathbf{r})\int_{S^2}\Theta(\hat{\mathbf{s}},\hat{\mathbf{s}}')\phi(\mathbf{r},\hat{\mathbf{s}}',t)\,\mathbf{d}\hat{\mathbf{s}} = q(\mathbf{r},\hat{\mathbf{s}},t),\ \mathbf{r}\in\Omega \tag{1}$$

where Ω is the domain of interest, c is the speed of light, $\hat{\mathbf{s}}$ is a unit vector in S^2, $\mu_{\mathrm{tr}} = \mu_{\mathrm{a}} + \mu_{\mathrm{s}}$ is the transport coefficient, μ_{a} is the absorption coefficient, μ_{s} is the scattering coefficient, $p(\hat{\mathbf{s}},\hat{\mathbf{s}}')$ is a normalised scattering phase function which represents the probability of scattering from $\hat{\mathbf{s}}$ to $\hat{\mathbf{s}}'$, q is a source of light, and $\phi(\mathbf{r},\hat{\mathbf{s}},t)$ is the radiance at a point $\mathbf{r}$, in direction $\hat{\mathbf{s}}$, at time t.

Suitable boundary conditions for the RTE enforce that the total energy inwards across the boundary is equal to that exiting the medium and reflected back into the domain, plus any sources on the boundary,

$$\int_{\hat{\mathbf{s}}\cdot\hat{\mathbf{n}}<0}\hat{\mathbf{s}}\phi(\mathbf{r},\hat{\mathbf{s}},t)\,\mathbf{d}\hat{\mathbf{s}} = \int_{\hat{\mathbf{s}}\cdot\hat{\mathbf{n}}>0}\hat{\mathbf{s}}R(\hat{\mathbf{s}})\phi(\mathbf{r},\hat{\mathbf{s}},t)\,\mathbf{d}\hat{\mathbf{s}} + q^{+}(\mathbf{r},\hat{\mathbf{s}},t),\ \mathbf{r}\in\delta\Omega \tag{2}$$

where $\delta\Omega$ is the boundary of the domain, $\hat{\mathbf{n}}$ is an outward normal to $\delta\Omega$ at $\mathbf{r}$, $R(\hat{\mathbf{s}})$ is an angularly dependent refraction coefficient, and q^{+} is a boundary source term.

2.1 Forward problem

In DOT a set of optical sources and detectors are placed on the boundary of the domain, and the measured flux across the boundary is recorded for each combination of source and detector. The forward problem is thus to find the data

$$g_{ij}(t) = \int_{\hat{\mathbf{s}}\cdot\hat{\mathbf{n}}<0} m_j(\mathbf{r},\hat{\mathbf{s}},t)\phi_i(\mathbf{r},\hat{\mathbf{s}},t)\,\mathbf{dr}\,\mathbf{d}\hat{\mathbf{s}}, \tag{3}$$

for all sources i, and detectors j, where $m(\mathbf{r},\hat{\mathbf{s}})$ is a spatially and angularly varying detection aperture, and the forward radiance field for the i^{th} source is given by

$$\phi_i(\mathbf{r},\hat{\mathbf{s}},t) = \mathcal{L}^{-1}q_i, \tag{4}$$

where $\mathcal{L}$ is an operator implementing the RTE of equation 1, for a given choice of parameters. For a set of sources and detectors we write the forward model

$$\mathbf{g}(t) = \mathcal{P}[\mu_{\mathrm{a}},\mu_{\mathrm{s}}](t), \tag{5}$$

where we have made explicit parameterisation by the optical properties of interest, μ_{a} and μ_{s}.

2.2 Inverse problem

The inverse problem in DOT is to infer the optical properties of interest (typically the absorption coefficient μ_{a}) from the measured data. Whilst arguably of less clinical relevance, the scattering coefficient μ_{s} may also be reconstructed. A typical approach is to pose this problem as the optimisation of a non-linear objective function,

$$\mathcal{E}(\mu_{\mathrm{a}},\mu_{\mathrm{s}}) = \frac{1}{2}\sum_{j,i}\int_{-\infty}^{\infty}\left(\frac{y_{j,i}(t) - \mathcal{P}_{j,i}[\mu_{\mathrm{a}},\mu_{\mathrm{s}}](t)}{\sigma_{j,i}}\right)^2\,\mathbf{d}t \tag{6}$$

the minimisation of which is consistent with a maximum likelihood estimation under the assumption that the data are corrupted with multivariate Gaussian noise.

The error functional of equation 6 is convex and differentiable, such that its minimisation can be achieved using a variety of non-linear first- and second-order non-linear optimisation techniques. The starting point in each case is a definition of the gradient of the error function, which in this case is given by

$$\frac{\partial\mathcal{E}}{\partial x} = -\sum_{j,i}\int_{-\infty}^{\infty}\left(\frac{y_{j,i}(t) - \mathcal{P}_{j,i}[\mu_{\mathrm{a}},\mu_{\mathrm{s}}](t)}{\sigma_{j,i}^2}\right)\left(\frac{\partial\mathcal{P}_{ji}[\mu_{\mathrm{a}},\mu_{\mathrm{s}}](t)}{\partial x}\right)\,\mathbf{d}t \tag{7}$$

where x is either μ_a or μ_s. The derivative of the forward operator with respect to the absorption and scattering coefficients is given by

$$\frac{\partial \mathcal{P}_{ji}[\mu_\mathrm{a},\mu_\mathrm{s}](t)}{\partial \mu_\mathrm{a}(\mathbf{r})} = -\int_{-\infty}^{\infty}\int_{S^2} \phi_j^*(\mathbf{r},\hat{\mathbf{s}},t')\phi_i(\mathbf{r},\hat{\mathbf{s}},t-t')\,\mathbf{d}\hat{\mathbf{s}}\,\mathbf{d}t', \tag{8}$$

and

$$\frac{\partial \mathcal{P}_{ji}[\mu_\mathrm{a},\mu_\mathrm{s}](t)}{\partial \mu_\mathrm{s}(\mathbf{r})} = \int_{-\infty}^{\infty}\left[\int_{S^2} \phi_j^*(\mathbf{r},\hat{\mathbf{s}},t')\phi_i(\mathbf{r},\hat{\mathbf{s}},t-t')\,\mathbf{d}\hat{\mathbf{s}} - \int_{S^2}\int_{S^2} \phi_j^*(\mathbf{r},\hat{\mathbf{s}}',t')p(\hat{\mathbf{s}},\hat{\mathbf{s}}')\phi_i(\mathbf{r},\hat{\mathbf{s}},t-t')\,\mathbf{d}\hat{\mathbf{s}}'\,\mathbf{d}\hat{\mathbf{s}}\right]\mathbf{d}t', \tag{9}$$

respectively, where ϕ_i is the solution of equation 1 for source i and ϕ_j^* is the solution of the adjoint equation,

$$\mathcal{L}^*\phi_j^* = 0 \quad \equiv \quad \left(-\frac{1}{c}\frac{\partial}{\partial t} - \hat{\mathbf{s}}\cdot\nabla + \mu_\mathrm{tr}\right)\phi_j^*(\mathbf{r},\hat{\mathbf{s}},t) - \mu_\mathrm{s}(\mathbf{r})\int_{S^2}\Theta(\hat{\mathbf{s}},\hat{\mathbf{s}}')\phi_j^*(\mathbf{r},\hat{\mathbf{s}}',t)\,\mathbf{d}\hat{\mathbf{s}}' = 0,\ \mathbf{r}\in\Omega \tag{10}$$

with the boundary conditions of equation 2 where the boundary source is given by

$$q_j^+(\mathbf{r},\hat{\mathbf{s}},t) = m_j(\mathbf{r},\hat{\mathbf{s}},t),\ \mathbf{r}\in\delta\Omega. \tag{11}$$

2.3 Discretisation

To represent the radiance numerically we discretise the spatio-angular-temporal radiance field ϕ in a piecewise-constant basis in space and time, and a truncated real spherical harmonic basis in angle. The discretised radiance field is thus expressed as

$$\phi(\mathbf{r},\hat{\mathbf{s}},t) = \sum_k^{N_k}\sum_p^{N_p}\sum_{\ell=0}^{N_\ell}\sum_{m=-\ell}^{\ell}\psi_{klmp}Y_{\ell m}(\hat{\mathbf{s}})\mathcal{X}_k^3(\mathbf{r})\mathcal{X}_p^1(t), \tag{12}$$

where $Y_{\ell m}$ (defined further in appendix A) are real spherical harmonics of degree ℓ, order m (with normalisaion condition $\langle Y_{\ell m}, Y_{\ell' m'}\rangle = \delta_{\ell\ell'}\delta_{mm'}$), and $\mathcal{X}^3$ and $\mathcal{X}^1$ are a suitable discretisation of the spatial domain in $\mathbb{R}^3$ and the temporal domain in $\mathbb{R}^1$, respectively.

The angular basis is limited to degree N_l which restricts the recording of high spatial frequencies inherently attenuated by the RTE in a highly scattering regime. Storage of the coefficient array ψ_{klmp} in this discretisation requires $N_kN_pN_t(N_l+1)^2$ elements. As an example, a spatial discretisation of 100^3 voxels, 100 time points, and an angular discretisation up to and including degree 4 implies 9×10^8 elements, requiring ~ 3.5Gb of storage in single-precision floating point.

2.3.1 Absorption sensitivity functions

To determine the sensitivity functions with respect to μ_a substitute equation 12 into equation 8,

$$\frac{\partial \mathcal{P}_{ji}[\mu_\mathrm{a},\mu_\mathrm{s}](t)}{\partial \mu_\mathrm{a}(\mathbf{r})} = -\int_{-\infty}^{\infty}\int_{S^2}\left[\sum_{k'}^{N_k}\sum_{p'}^{N_p}\sum_{\ell'=0}^{N_\ell}\sum_{m'=-\ell}^{\ell}\psi'_{k'l'm'p'}Y_{\ell'm'}(\hat{\mathbf{s}})\mathcal{X}_{k'}^3(\mathbf{r})\mathcal{X}_{p'}^1(t')\right] \times\left[\sum_k^{N_k}\sum_p^{N_p}\sum_{\ell=0}^{N_\ell}\sum_{m=-\ell}^{\ell}\psi_{klmp}Y_{\ell m}(\hat{\mathbf{s}})\mathcal{X}_k^3(\mathbf{r})\mathcal{X}_p^1(t-t')\right]\mathbf{d}\hat{\mathbf{s}}\,\mathbf{d}t'. \tag{13}$$

The real spherical harmonic basis used in this work forms an orthonormal basis,

$$\int_{S^2} Y_{\ell m}(\hat{\mathbf{s}})Y_{\ell' m'}(\hat{\mathbf{s}})\,\mathbf{d}\hat{\mathbf{s}} = \delta_{\ell\ell'}\delta_{mm'}, \tag{14}$$

such that

$$\frac{\partial \mathcal{P}_{ji}[\mu_\mathrm{a},\mu_\mathrm{s}](t)}{\partial \mu_\mathrm{a}(\mathbf{r})} = -\sum_{\ell=0}^{N_\ell}\sum_{m=-\ell}^{\ell}\int_{-\infty}^{\infty}\left[\sum_{k'}^{N_k}\sum_{p'}^{N_p}\psi'_{k'lmp'}\mathcal{X}_{k'}^3(\mathbf{r})\mathcal{X}_{p'}^1(t')\right]\left[\sum_k^{N_k}\sum_p^{N_p}\psi_{klmp}\mathcal{X}_k^3(\mathbf{r})\mathcal{X}_p^1(t-t')\right]\mathbf{d}t'. \tag{15}$$

For the purposes of optimisation we wish to represent the sensitivity functions as a set of coefficients in a suitable basis. In this work we choose to represent the parameter distributions of interest in the same spatial basis as the radiance field. We accordingly project the resultant sensitivity functions into the same spatial and temporal basis as the radiance field,

$$\frac{\partial \mathcal{P}_{ji}[\mu_\mathrm{a},\mu_\mathrm{s}]_p}{\partial \mu_{\mathrm{a}k}} = \int_{-\infty}^{\infty}\int_{\Omega} \mathcal{X}_k^3(\mathbf{r})\mathcal{X}_p^1(t)\frac{\partial \mathcal{P}_{ji}[\mu_\mathrm{a},\mu_\mathrm{s}](t)}{\partial \mu_\mathrm{a}(\mathbf{r})}\,\mathbf{dr}\,\mathbf{d}t \tag{16}$$

which, for our choice of a piecewise-constant non-overlapping uniform rectilinear basis, is given by,

$$\frac{\partial \mathcal{P}_{ji}[\mu_\mathrm{a},\mu_\mathrm{s}]_p}{\partial \mu_{\mathrm{a}k}} = -\sum_{\ell=0}^{N_\ell}\sum_{m=-\ell}^{\ell}\sum_{q=0}^{p}\Delta r\Delta t\,\psi'_{klm(p-q)}\psi_{klmq} \tag{17}$$

where $\Delta r = \int \mathcal{X}_k^3(\mathbf{r})\,\mathbf{dr}$ and $\Delta t = \int \mathcal{X}_k^1(t)\,\mathbf{d}t$ for any k, it is assumed that the source functions are delta functions in time, and $p = 0, 1, \ldots, N_t - 1$, for recording over the period $0 \le t \le N_t\Delta t$.

2.3.2 Scattering sensitivity functions

To determine the sensitivity functions with respect to μ_s we begin by expressing the Henyey-Greenstein phase function $\Theta(\hat{\mathbf{s}},\hat{\mathbf{s}}')$ in the same spherical harmonic basis as that in which we represent the radiance, whereby it forms a series in powers of the anisotropy factor g,[17]

$$\Theta(\hat{\mathbf{s}},\hat{\mathbf{s}}') = \sum_{\ell=0}^{\infty}\sum_{m=-\ell}^{\ell} g^\ell Y_{\ell m}(\hat{\mathbf{s}})Y_{\ell m}(\hat{\mathbf{s}}), \tag{18}$$

and now substitute equations 12 and 18 into the second term of equation 9,

$$\begin{aligned}\int_{S^2}\int_{S^2} \phi_j^*(\mathbf{r},\hat{\mathbf{s}}',t')\Theta(\hat{\mathbf{s}},\hat{\mathbf{s}}')\phi_i(\mathbf{r},\hat{\mathbf{s}},t-t')\,\mathbf{d}\hat{\mathbf{s}}'\,\mathbf{d}\hat{\mathbf{s}}&\\ = \int_{S^2}\int_{S^2}\left[\sum_{k'}^{N_k}\sum_{p'}^{N_p}\sum_{\ell'=0}^{N_\ell}\sum_{m'=-\ell}^{\ell}\psi'_{k'l'm'p'}Y_{\ell'm'}(\hat{\mathbf{s}}')\mathcal{X}_{k'}^3(\mathbf{r})\mathcal{X}_{p'}^1(t')\right]&\\ \times\left[\sum_{\ell''=0}^{\infty}\sum_{m''=-\ell''}^{\ell''} g^{\ell''}Y_{\ell''m''}(\hat{\mathbf{s}})Y_{\ell''m''}(\hat{\mathbf{s}}')\right]&\\ \times\left[\sum_{k}^{N_k}\sum_{p}^{N_p}\sum_{\ell=0}^{N_\ell}\sum_{m=-\ell}^{\ell}\psi_{klmp}Y_{\ell m}(\hat{\mathbf{s}})\mathcal{X}_k^3(\mathbf{r})\mathcal{X}_p^1(t-t')\right]\mathbf{d}\hat{\mathbf{s}}'\,\mathbf{d}\hat{\mathbf{s}}.&\end{aligned} \tag{19}$$

The integrals in the expression can be separated by defining

$$I_1 = \int_{S^2} I_2(\hat{\mathbf{s}})\left[\sum_{k}^{N_k}\sum_{p}^{N_p}\sum_{\ell=0}^{N_\ell}\sum_{m=-\ell}^{\ell}\psi_{klmp}Y_{\ell m}(\hat{\mathbf{s}})\mathcal{X}_k^3(\mathbf{r})\mathcal{X}_p^1(t-t')\right]\mathbf{d}\hat{\mathbf{s}} \tag{20}$$

where

$$I_2 = \int_{S^2}\left[\sum_{k'}^{N_k}\sum_{p'}^{N_p}\sum_{\ell'=0}^{N_\ell}\sum_{m'=-\ell}^{\ell}\psi'_{k'l'm'p'}Y_{\ell'm'}(\hat{\mathbf{s}}')\mathcal{X}_{k'}^3(\mathbf{r})\mathcal{X}_{p'}^1(t')\right]\left[\sum_{\ell''=0}^{\infty}\sum_{m''=-\ell''}^{\ell''} g^{\ell''}Y_{\ell''m''}(\hat{\mathbf{s}})Y_{\ell''m''}(\hat{\mathbf{s}}')\right]\mathbf{d}\hat{\mathbf{s}}'. \tag{21}$$

We invoke the orthogonality relationship for the real spherical harmonics, which reduces the integral over $\hat{\mathbf{s}}'$

$$I_2 = \sum_{k'}^{N_k}\sum_{p'}^{N_p}\sum_{\ell'=0}^{\infty}\sum_{m'=-\ell'}^{\ell'}\psi'_{k'l'm'p'}g^{\ell'}Y_{\ell'm'}(\hat{\mathbf{s}})\mathcal{X}_{k'}^3(\mathbf{r})\mathcal{X}_{p'}^1(t'), \tag{22}$$

and substitute the result into the expression for I_1

$$I_1 = \int_{S^2} \left[\sum_{k'}^{N_k} \sum_{p'}^{N_p} \sum_{\ell'=0}^{\infty} \sum_{m'=-\ell'}^{\ell'} \psi'_{k'l'm'p'} g^{\ell'} Y_{\ell'm'}(\hat{\mathbf{s}}') \mathcal{X}^3_{k'}(\mathbf{r}) \mathcal{X}^1_{p'}(t') \right] \left[\sum_{k}^{N_k} \sum_{p}^{N_p} \sum_{\ell=0}^{N_\ell} \sum_{m=-\ell}^{\ell} \psi_{klmp} Y_{\ell m}(\hat{\mathbf{s}}) \mathcal{X}^3_{k}(\mathbf{r}) \mathcal{X}^1_{p}(t-t') \right] \mathbf{d}\hat{\mathbf{s}}' \tag{23}$$

where the integral is again resolved by the orthogonality relation,

$$I_1 = \sum_{\ell=0}^{\infty} \sum_{m=-\ell}^{\ell} \left[\sum_{k'}^{N_k} \sum_{p'}^{N_p} \psi'_{k'lmp'} g^{\ell} \mathcal{X}^3_{k'}(\mathbf{r}) \mathcal{X}^1{}_{p'}(t') \sum_{k}^{N_k} \sum_{p}^{N_p} \psi_{klmp} \mathcal{X}^3_{k}(\mathbf{r}) \mathcal{X}^1_{p}(t-t') \right]. \tag{24}$$

We now insert 24 into equation 9, where we note that the first term is given by the earlier result for the absorption gradient as expressed in equation 15,

$$\begin{aligned} \frac{\partial \mathcal{P}_{ji}[\mu_\mathrm{a}, \mu_\mathrm{s}](t)}{\partial \mu_\mathrm{s}(\mathbf{r})} = \sum_{\ell=0}^{\infty} \sum_{m=-\ell}^{\ell} \int_{-\infty}^{\infty} & \left[\sum_{k'}^{N_k} \sum_{p'}^{N_p} \psi'_{k'lmp'} \mathcal{X}^3_{k'}(\mathbf{r}) \mathcal{X}^1_{p'}(t') \sum_{k}^{N_k} \sum_{p}^{N_p} \psi_{klmp} \mathcal{X}^3_{k}(\mathbf{r}) \mathcal{X}^1_{p}(t-t') \right] \\ & - \left[\sum_{k'}^{N_k} \sum_{p'}^{N_p} \psi'_{k'lmp'} g^{\ell} \mathcal{X}^3_{k'}(\mathbf{r}) \mathcal{X}^1_{p'}(t') \sum_{k}^{N_k} \sum_{p}^{N_p} \psi_{klmp} \mathcal{X}^3_{k}(\mathbf{r}) \mathcal{X}^1_{p}(t-t') \right] \mathbf{d}t' \end{aligned} \tag{25}$$

which is readily factorised

$$\frac{\partial \mathcal{P}_{ji}[\mu_\mathrm{a}, \mu_\mathrm{s}](t)}{\partial \mu_\mathrm{s}(\mathbf{r})} = \sum_{\ell=1}^{\infty} \sum_{m=-\ell}^{\ell} \int_{-\infty}^{\infty} \left[\sum_{k'}^{N_k} \sum_{p'}^{N_p} \psi'_{k'lmp'} \mathcal{X}^3_{k'}(\mathbf{r}) \mathcal{X}^1_{p'}(t') \sum_{k}^{N_k} \sum_{p}^{N_p} \psi_{klmp} \mathcal{X}^3_{k}(\mathbf{r}) \mathcal{X}^1_{p}(t-t') \right] (1-g^{\ell}) \, \mathbf{d}t'. \tag{26}$$

where since for the zeroth degree spherical harmonics $(1 - g^\ell) = 0$, the limits of the first summation have been altered, and it is now readily apparent that the gradient with respect to scattering contains contributions only from the gradient of the field, and not its average.

Finally we project this result into the reconstruction basis,

$$\frac{\partial \mathcal{P}_{ji}[\mu_\mathrm{a}, \mu_\mathrm{s}]_p}{\partial \mu_{\mathrm{s}k}} = -\sum_{\ell=1}^{N_\ell} \sum_{m=-\ell}^{\ell} \sum_{q=0}^{p} \Delta r \Delta t \, \psi'_{klm(p-q)} \psi_{klmq} (1 - g^{\ell}), \tag{27}$$

where $\Delta r = \int \mathcal{X}^3_k(\mathbf{r}) \, \mathbf{d}\mathbf{r}$ and $\Delta t = \int \mathcal{X}^1_k(t) \, \mathbf{d}t$ for any k, it is assumed that the source functions are delta functions in time, and $p = 0, 1, \ldots, N_t - 1$, for recording over the period $0 \leq t \leq N_t \Delta t$.

3. METHOD

In this work, we use the Monte-Carlo method to approximate the forward and adjoint RTE operators in order to build the gradients of the forward model according to equations 17 and 27.

3.1 Monte-Carlo forward solver

We have developed a Monte-Carlo forward solver which employs full ray-tracing of the computational domain in which all parameters (absorption, scattering, refractive index) are defined on the same basis as the radiance field. The front-end simulation code is written in the Julia language,[21] which controls and dispatches the execution of kernels on both the CPU (written in Julia), and the GPU (written in nVidia's CUDA language).

The code computes step lengths and scales radiance deposition according to the alebdo-weight (AW) method.[16] The roulette technique employed in the MCML package[7] is used to reduce variance and improve computational efficiency. At each deposition event the vector of radiance basis coefficients $\vec{\psi}$ is updated

$$\psi_{klmp} \leftarrow \psi_{klmp} + \Delta w \Delta \phi_{klmp}, \tag{28}$$

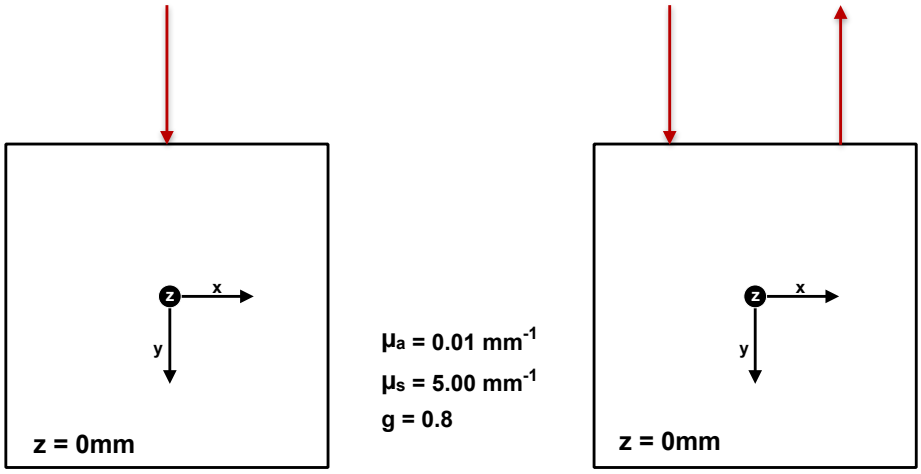

Figure 1. Homogenous domain of dimensions $50 \times 50 \times 50$mm, absorption coefficient $\mu_{\mathrm{a}} = 0.01\mathrm{mm}^{-1}$, scattering coefficient $\mu_{\mathrm{s}} = 5.00\mathrm{mm}^{-1}$, ansiotropy factor $g = 0.8$. Inwards arrows depict the source locations for radiance evaluations (left), and gradient calculations (right). Outwards arrows indicate detector location for gradient evaluations (right only).

where Δw is computed according to the AW technique, and

$$\Delta\phi_{klmp} = \int_{-\infty}^{\infty}\int_{\Omega}\int_{S2} f(\mathbf{r},\hat{\mathbf{s}},t)Y_{\ell m}(\hat{\mathbf{s}})\mathcal{X}_k^3(\mathbf{r})\mathcal{X}_p^1(t)\,\mathbf{d}\hat{\mathbf{s}}\,\mathbf{dr}\,\mathbf{d}t \tag{29}$$

with

$$f(\mathbf{r},\hat{\mathbf{s}},t) = \delta(\mathbf{r}-\mathbf{r}')\delta(\hat{\mathbf{s}}-\hat{\mathbf{s}}')\delta(t-t'), \tag{30}$$

for deposition by a photon packet at location $\mathbf{r}'$, travelling in direction $\hat{\mathbf{s}}'$, having travelled for t'.

Source functions, measurement apertures, and adjoint source functions are directly implemented by specification of their spatial, angular, and temporal probability density functions. When acting as sources, these functions are sampled uniformly to initialise the location, direction, and start time of a given photon packet. When acting as detectors, the values of the probability density functions are calculated at the specified location, direction, and time, and a weighted fraction of the incoming flux is deposited accordingly.

4. RESULTS

To explore our proposed technique, we present sensitivity calculated functions according to the presented theory. We consider the CW case in depth, in both an homogeneous domain and one containing a void region. In each case we consider the variation of the sensitivity functions with respect to the degree of the angular discretisation.

4.1 Homogenous domain

We first consider an homogenous cube, as depicted in figure 1.

To evaluate the forward radiance distribution we add a single pencil-source at the center of the boundary in the $x-z$ plane, as depicted in figure 1 (left). In figure 2 we plot the spherical harmonic coefficient values for the resultant radiance distribution, evaluated in the $y-z$ plane in the axis of the source. The $Y_{0,0}$ component is by definition the fluence in the medium, and follows the expected exponential decay profile away from the source. The $Y_{1,-1}$ component (second row, left) corresponds to the gradient of the fluence in the $+x$ direction, and demonstrates that the field decays from the peak generated by the pencil source at $x = 0$. The $Y_{1,0}$ component (second row, center) corresponds to the gradient of the fluence in the $+z$ direction — this is zero throughout the image since we are observing the gradient in the plane of the source, where the fluence is at

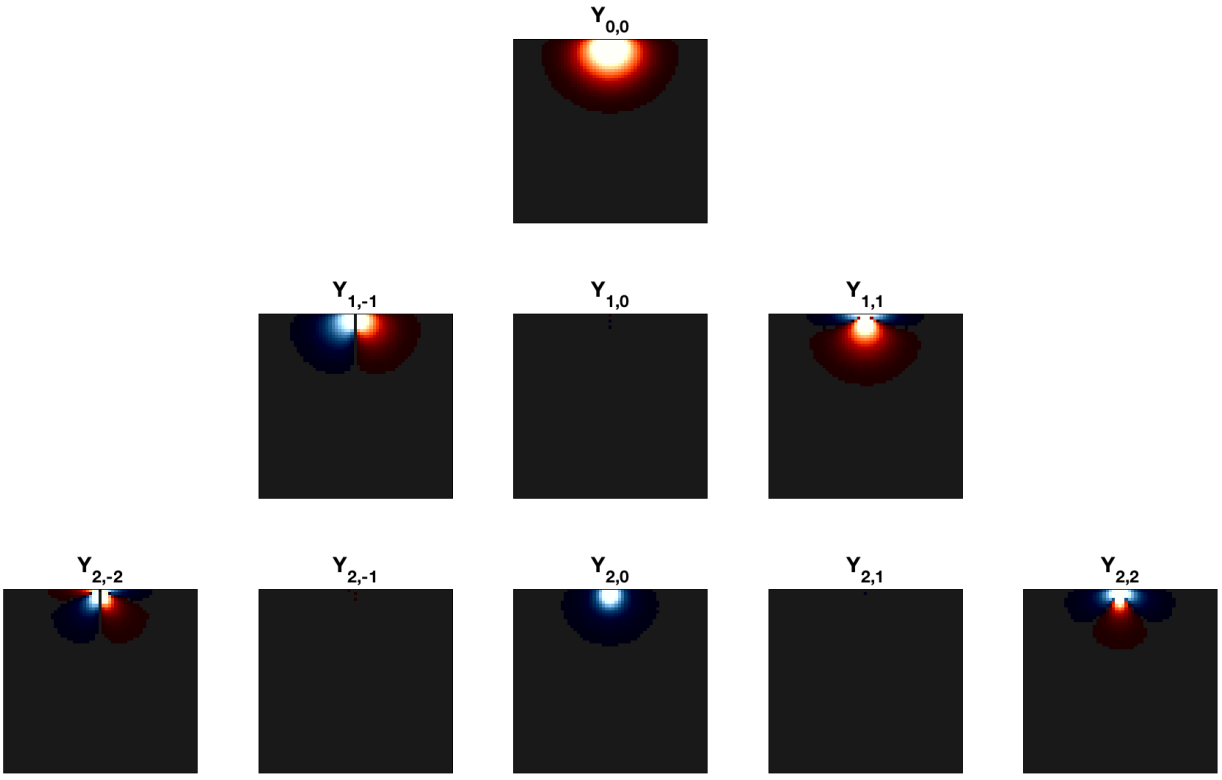

Figure 2. Forward radiance fields in an homogenous cube for a single pencil source as depicted in figure 1. All plots share a common, arbitrary, colour scale, red indicates positive values, blue indicated negative. Fields are shown in a slice through the plane of the source.

an extremum. The $Y_{1,-1}$ component represents the gradient of the fluence in the $+y$ direction. At depth the gradient is seen to be positive, representing the decay of the fluence into the medium. Close to the boundary we find the gradient is negative, representing the backscattering of light towards the input plane. Since the higher harmonics contain combinations of the Cartesian components they do not offer a simple interpretation, though we note that the magnitude of the higher harmonics decays more quickly with respect to depth, as the scattering process randomises the direction of the propagation of the direction of the light.

We now proceed to evaluate the absorption and scattering sensitivity functions in the same domain. To this end, we add a single source-detector pair to the domain, as depicted in figure 1 (right). Figure 3 depicts the sensitivity functions for the absorption coefficient, evaluated using different maximum degress of spherical harmonic coefficients, and the difference between them (multiplied by ten). The absorption sensitivity functions form the familiar 'banana' shaped distribution with peak sensitivity near the source and detector. Given the scaling of the difference, we find that for the homogenous domain their is limited benefit to increasing the degree of the spherical harmonic expansion.

Figure 4 depicts the sensitivity functions for the scattering coefficient, in the same configuration. The form of the scattering coefficient is more complex, and demonstrates a bipolar distribution. At depth the common 'banana' shaped sensitivity function is evident, though closer to the boundary we see a region of positive sensitivity in which an increase in the scattering coefficient will cause more light to reach the detector from the source position, by increased scattering of the incident light. As in the case of absorption, increasing the degree of spherical harmonic expansion used to represent the field has limited effect, excepting regions very close to the source and detector.

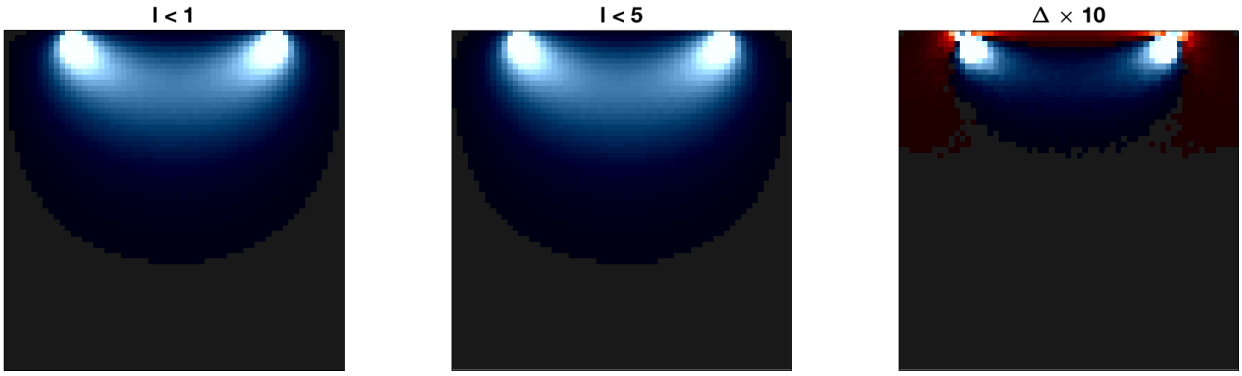

Figure 3. Sensitivity functions for the absorption coefficient in an homogenous cube, built using spherical harmonic functions of degree $\ell \leq 1$ (left) and $\ell \leq 4$ (centre), and the difference between the two results (right). The scale of the difference plot is multiplied by ten relative to the sensitivity functions

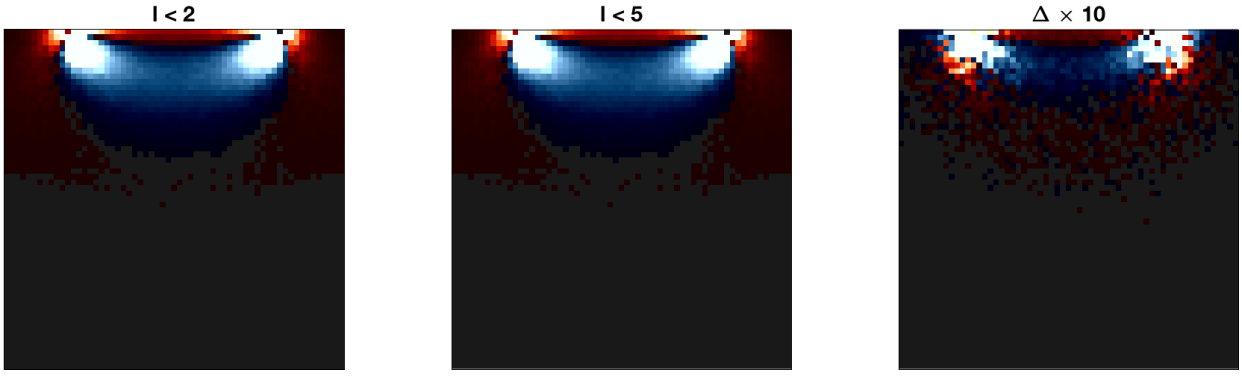

Figure 4. Sensitivity functions for the scattering coefficient in an homogenous cube, built using spherical harmonic functions of degree $\ell \leq 2$ (left) and $\ell \leq 4$ (centre), and the difference between the two results (right). The scale of the difference plot is multiplied by ten relative to the sensitivity functions

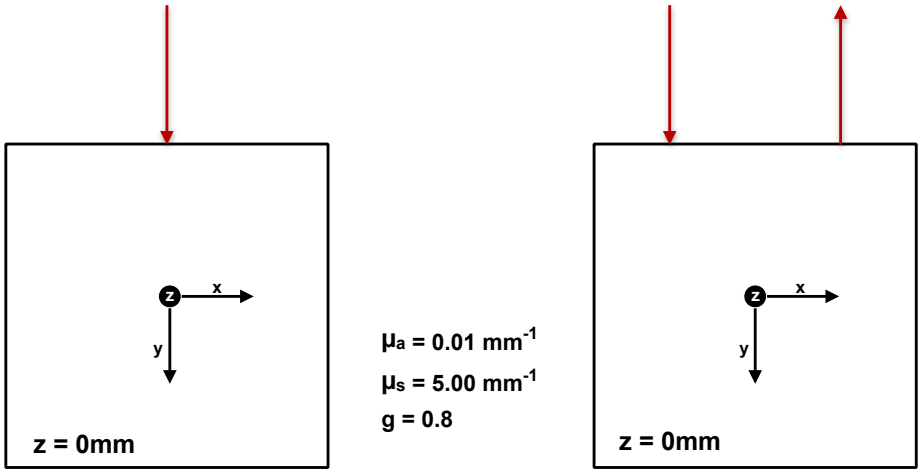

Figure 5. Domain including a void of dimensions $50 \times 50 \times 50$mm, bulk absorption coefficient $\mu_a = 0.01\text{mm}^{-1}$, scattering coefficient $\mu_s = 5.00\text{mm}^{-1}$, and ansiotropy factor $g = 0.8$. The void region has scattering coefficient $\mu_s = 0.1\text{mm}^{-1}$. Inwards arrows depict the source locations for radiance evaluations (left), and gradient calculations (right). Outwards arrows indicate detector location for gradient evaluations (right only).

4.2 Domain with a void region

We now consider a a domain containing a void region, as depicted in figure 5.

We once again illuminate the medium with a single pencil-source at the center of the boundary in the $x - z$ plane, as depicted in figure 5 (left). In figure 6 we plot the spherical harmonic coefficient values for the resultant radiance distribution, evaluated in the $y - z$ plane in the axis of the source. In the presence of a void region, significant differences are evident relative to the homogenous case. The lack of scattering in the void is such that the direction of transport is not randomised to as great an extent as in the homogenous case, this allows propagation of the higher harmonics far deeper into the medium.

Following the addition of a source-detector pair to the domain, as depicted in figure 5 (right), we compute the absorption and scattering sensitivity functions in the domain. Figure 7 depicts the sensitivity functions for the absorption coefficient, evaluated using different maximum degress of spherical harmonic coefficients, and the difference between them, presented on the same scale. The void region supports the collimation of the source until far deeper into the domain, reducing the sensitivity to absorption near the surface of the domain. Of particular note is that the difference between a zeroth- and fourth-degree spherical harmonic approximation is now far more pronounced: with a higher degree approximation the collimation of the input is better captured, leading to reduced superficial sensitivity.

Figure 8 depicts the sensitivity functions for the scattering coefficient, in the same configuration. Again it is demonstrated that in the presence of a void region, there are significant differences in the sensitivity functions. In particular, we note that a higher degree approximation allows backscatering from the highly scattering region below the void to lead to a band of higher (more positive) sensitivity whereby backscattering from the region back into the void layer increases the detected signal. We will return to this point in the following section.

5. DISCUSSION & CONCLUSIONS

We have demonstrated a new technique to stochastically estimate solutions to the radiative transport equation in arbitrary three dimensional domains. This method naturally provides estimates of the radiance in a spherical harmonic basis. Following their derivation, the derivatives of the RTE with respect to absorption and scattering parameters are shown to have a straightforward form in this choice of discretisation.

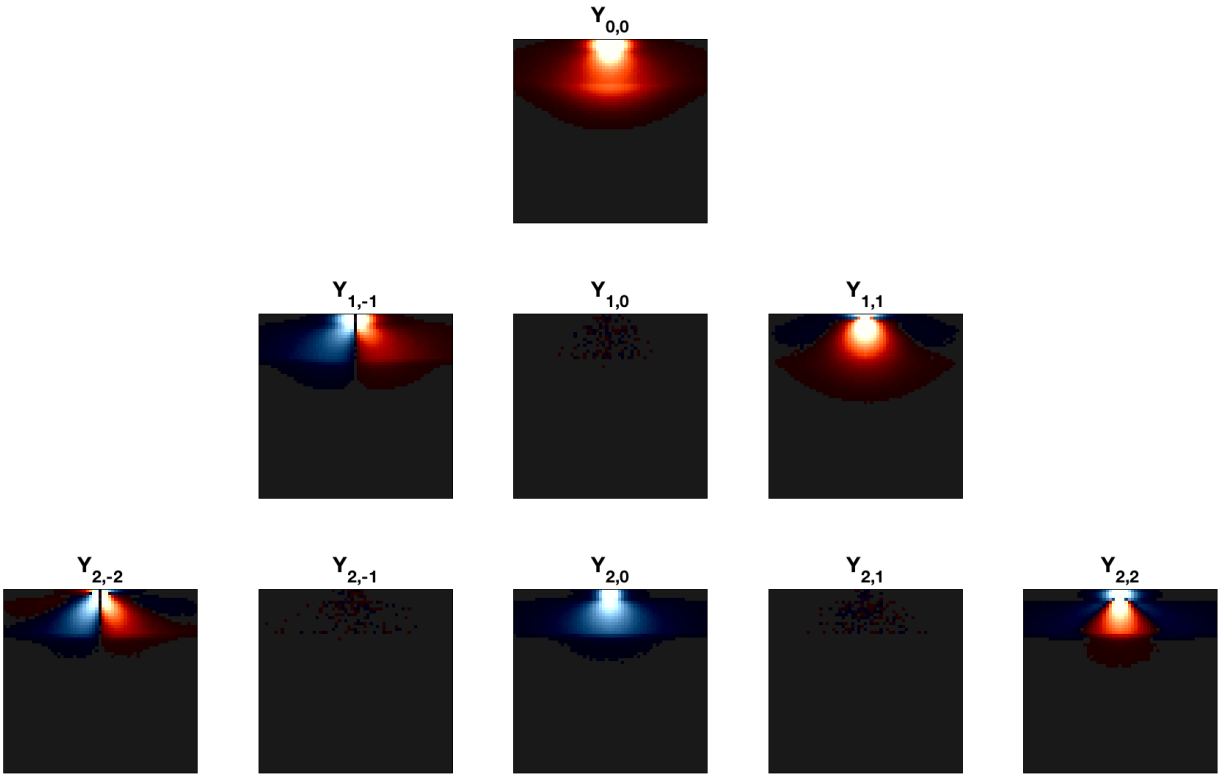

Figure 6. Forward radiance fields in an homogenous cube for a single pencil source as depicted in figure 5. All plots share a common, arbitrary, colour scale, red indicates positive values, blue indicated negative. Fields are shown in a slice through the plane of the source.

We have shown the form of sensitivity functions calculated in an homogenous cube, and those in the presence of a void region. As expected, the presence of a void region allows higher degree harmonic components to penetrate deeper into the domain, thus requiring a higher degree spherical harmonic expansion for their representation. These derivatives are the starting point of the inverse problem which seeks to recover the parameters of interest from measurements.

The use of the RTE overcomes approximations present in the diffusion equation which permits accurate calculation of the optical field in the presence of short source-detector separations, and void regions. If required, stochastic solution of the RTE allows computation of the time-domain form of both the forward radiance fields and the sensitivity functions without extra computational cost over the CW case.

ACKNOWLEDGMENTS

This research was funded with support from EPSRC grants EP/J021318/1, EP/N032055/1 and EPSRC Medical Imaging CDT Imaging, EP/L01641/78. S. Powell acknowledges support from RAEng Fellowship RF1516\15\33. The authors declare they have no conflicts of interest, financial or otherwise, relevant to this manuscript. The authors acknowledge the contribution of Andre Liemert who provided data used in the validation of RMC. The authors thank Tanja Tarvainen for useful discussions regarding the forward model and inversion.

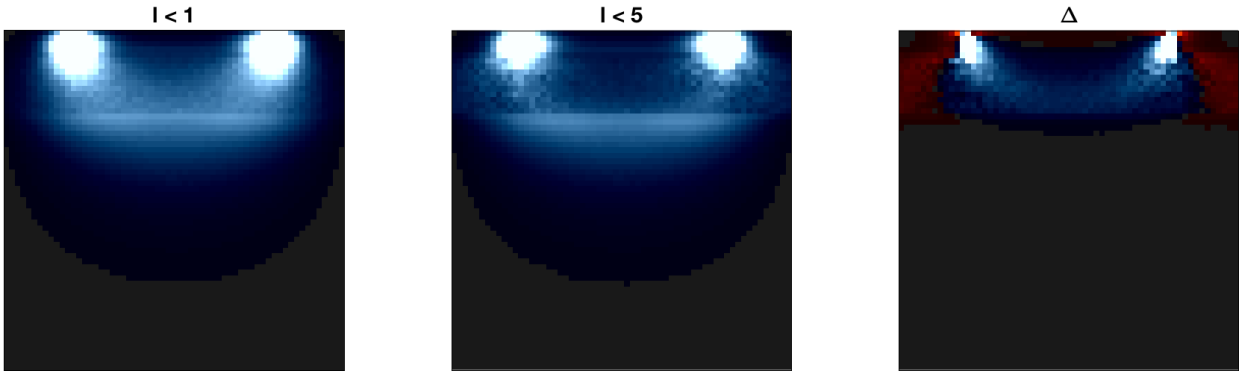

Figure 7. Sensitivity functions for the absorption coefficient in a cube with a void region, built using spherical harmonic functions of degree $\ell \leq 1$ (left) and $\ell \leq 4$ (centre), and the difference between the two results (right). The colour scale is identical for all plots.

Figure 8. Sensitivity functions for the scattering coefficient in a cube with a void region, built using spherical harmonic functions of degree $\ell \leq 2$ (left) and $\ell \leq 4$ (centre), and the difference between the two results (right). The colour scale is identical for all plots.

APPENDIX A. REAL SPHERICAL HARMONICS

The spherical harmonics are a set of complex-valued functions which form an orthogonal basis over the sphere. For computational convenience we choose to use the real-valued form of this set,

$$Y_{\ell m} = \begin{cases} \sqrt{2}\sqrt{\frac{(2\ell+1)}{4\pi}}\sqrt{\frac{(\ell-|m|)!}{(\ell+|m|)!}}P_\ell^{|m|}(\cos\theta)\sin|m|\varphi & \text{if } m<0 \\ \sqrt{\frac{(2\ell+1)}{4\pi}}P_\ell^m(\cos\theta) & \text{if } m=0 \\ \sqrt{2}\sqrt{\frac{(2\ell+1)}{4\pi}}\sqrt{\frac{(\ell-m)!}{(\ell+m)!}}P_\ell^m(\cos\theta)\cos m\varphi & \text{if } m>0 \end{cases} \tag{31}$$

where ℓ is the degree of the spherical harmonic, m is the order, P_ℓ^m are the associated Legendre polynomials.

REFERENCES

[1] S. Arridge, "Optical tomography in medical imaging," *Inverse problems* **15**, pp. R41–R93, 1999.

[2] T. Tarvainen, M. Vauhkonen, V. Kolehmainen, and J. Kaipio, "Hybrid radiative–transfer–diffusion model for optical tomography", *Appl Opt* **44 (6)**, pp. 876886, 2005 .

[3] T. Tarvainen, M. Vauhkonen, V. Kolehmainen, S. Arridge, and J. Kaipio, "Coupled radiative transfer equation and diffusion approximation model for photon migration in turbid medium with low-scattering and nonscattering regions", *Phys Med Biol*, **50** pp. 49134930, 2005.

[4] T. Tarvainen, M. Vauhkonen, V. Kolehmainen, and J. Kaipio, "Finite element model for the coupled radiative transfer equation and diffusion approximation", *Int J Numer Meth Engng*, **65 (3)**, pp. 383405, 2006.

[5] T. Tarvainen, *Computational Methods for Light Transport in Optical Tomography.* PhD thesis, University of Kuopio, 2006.

[6] P. Surya Mohan, T. Tarvainen, M. Schweiger, A. Pulkkinen, and S. R. Arridge, "Variable order spherical harmonic expansion scheme for the radiative transport equation using finite elements," *Journal of Computational Physics* **230**, pp. 7364–7383, Aug. 2011.

[7] L. Wang, S. Jacques, and L. Zheng, "MCML–Monte Carlo modeling of light transport in multi-layered tissues," *Computer methods and programs in biomedicine* **47**, pp. 131–146, 1995.

[8] D. Boas, J. Culver, J. Stott, and A. Dunn, "Three dimensional Monte Carlo code for photon migration through complex heterogeneous media including the adult human head," *Optics express* **10**, pp. 159–70, Feb. 2002.

[9] Q. Fang and D. A. Boas, "Monte Carlo simulation of photon migration in 3D turbid media accelerated by graphics processing units," *Optics Express* **17**, pp. 20178–90, Oct. 2009.

[10] S. Powell and T. S. Leung, "Highly parallel Monte-Carlo simulations of the acousto-optic effect in heterogeneous turbid media.," *Journal of Biomedical Optics* **17**, p. 045002, Apr. 2012.

[11] M.-R. Antonelli, A. Pierangelo, T. Novikova, P. Validire, A. Benali, B. Gayet, and A. De Martino, "Impact of model parameters on Monte Carlo simulations of backscattering Mueller matrix images of colon tissue.," *Biomedical Optics Express* **2**, pp. 1836–51, July 2011.

[12] N. Manuchehrabadi, Y. Chen, A. Lebrun, R. Ma, and L. Zhu, "Computational simulation of temperature elevations in tumors using Monte Carlo method and comparison to experimental measurements in laser photothermal therapy.," *Journal of Biomechanical Engineering* **135**, p. 121007, Dec. 2013.

[13] J. Cassidy, V. Betz, and L. Lilge, "Treatment plan evaluation for interstitial photodynamic therapy in a mouse model by Monte Carlo simulation with FullMonte," *Frontiers in Physics* **3**, pp. 1–10, Feb. 2015.

[14] C. Zhu and Q. Liu, "Review of Monte Carlo modeling of light transport in tissues," *Journal of Biomedical Optics* **18**, p. 50902, May 2013.

[15] Q. Fang, "Mesh-based Monte Carlo method using fast ray-tracing in Plücker coordinates," *Biomedical Optics Express* **1**, pp. 165–75, Aug. 2010.

[16] A. Sassaroli and F. Martelli, "Equivalence of four Monte Carlo methods for photon migration in turbid media.," *Journal of the Optical Society of America. A, Optics, Image Science, and Vision* **29**, pp. 2110–7, Oct. 2012.

[17] J. Heino, S. Arridge, J. Sikora, and E. Somersalo, "Anisotropic effects in highly scattering media," *Physical Review E* **68**, pp. 1–8, Sept. 2003.

[18] W. Star, J. Marijnissen, and M. Gemert, "Light dosimetry in optical phantoms and in tissues: I. Multiple flux and transport theory," *Physics in Medicine and Biology* **33**(4), p. 437, 1988.

[19] R. Hochuli, S. Powell, S. Arridge, and B. Cox, "Forward and adjoint radiance Monte Carlo models for quantitative photoacoustic imaging," in *Proc. of SPIE, Photons Plus Ultrasound: Imaging and Sensing*, A. A. Oraevsky and L. V. Wang, eds., **9323**, pp. 93231P–10, Mar. 2015.

[20] R. Hochuli, *Monte Carlo Methods in Quantitative Photoacoustic Tomography*. PhD thesis, University College London, 2016.

[21] J. Bezanson, A. Edelman, S. Karpinski, and V. B. Shah, "Julia: A Fresh Approach to Numerical Computing," *arXiv* **1411.1607**, p. 37, Nov. 2014.

[22] M. J. C. Van Gemert, A. J. Welch, W. M. Star, M. Motamedi, and W.-F. Cheong, "Tissue optics for a slab geometry in the diffusion approximation," *Lasers in Medical Science* **2**, pp. 295–302, Dec. 1987.

[23] A. K. Jha, M. A. Kupinski, H. H. Barrett, E. Clarkson, and J. H. Hartman, "Three-dimensional Neumann-series approach to model light transport in nonuniform media.," *Journal of the Optical Society of America. A, Optics, image science, and vision* **29**, pp. 1885–99, Sept. 2012.

[24] L. Henyey and J. Greenstein, "Diffuse radiation in the galaxy," in *Annales d'Astrophysique*, **3**, pp. 70–84, 1940.